14. Buffett, B. A., Huppert, H. E., Lister, J. R. & Woods, A. W. On the thermal evolution of the Earth's core. *J. Geophys. Res.* **101,** 7989–8006 (1996).
15. Stevenson, D. J. Mars' core and magnetism. *Nature* **412,** 214–219 (2001).
16. Roberts, P. H. & Soward, A. M. Dynamo theory. *Annu. Rev. Fluid Mech.* **24,** 459–512 (1992).
17. Williams, J. G., Boggs, D. H., Yoder, C. F. & Ratcliff, J. T. Lunar rotational dissipation in solid body and molten core. *J. Geophys. Res.* **106,** 27933–27968 (2001).
18. Bunge, H.-P. & Baumgardner, J. R. Mantle convection modeling on parallel virtual machines. *Comput. Phys.* **9,** 207–215 (1995).
19. Yang, W.-S. & Baumgardner, J. R. A matrix-dependent transfer multigrid method for strongly variable viscosity infinite Prandtl number thermal convection. *Geophys. Astrophys. Fluid* **92,** 151–195 (2000).
20. Christensen, U. R. Heat transport by variable viscosity convection and implications for the Earth's thermal evolution. *Phys. Earth Planet. Inter.* **35,** 264–282 (1984).
21. Moresi, L.-N. & Solomatov, V. S. Numerical investigation of 2D convection with extremely large viscosity variations. *Phys. Fluids* **7,** 2154–2162 (1995).
22. Jellinek, A. M., Lenardic, A. & Manga, M. The influence of interior mantle temperature on the structure of plumes: Heads for Venus, tails for Earth. *Geophys. Res. Lett.* **29,** doi:10.1029/2001GL014624 (2002).
23. Davaille, A. Simultaneous generation of hotspots and superswells by convection in a heterogeneous planetary mantle. *Nature* **402,** 756–760 (1999).
24. Gonnermann, H. M., Manga, M. & Jellinek, A. M. Dynamics and longevity of an initially stratified mantle. *Geophys. Res. Lett.* **29,** doi:10.1029/2002GL01485 (2002).
25. Hood, L. L., Mitchell, D. L., Lin, R. P., Acuna, M. H. & Binder, A. B. Initial measurements of the lunar induced magnetic dipole moment using Lunar Prospector magnetometer data. *Geophys. Res. Lett.* **26,** 2327–2330 (1999).
26. Jolliff, B. L., Gillis, J. J., Haskin, L. A., Korotev, R. L. & Wieczorek, M. A. Major lunar crustal terranes: Surface expressions and crust–mantle origins. *J. Geophys. Res.* **105,** 4197–4216 (2000).
27. Haskin, L. A., Gillis, J. J., Korotev, R. L. & Jolliff, B. L. The materials of the lunar Procellarum KREEP Terrane: A synthesis of data from geomorphological mapping, remote sensing, and sample analyses. *J. Geophys. Res.* **105,** 20403–20415 (2000).
28. Delano, J. Pristine lunar glasses: Criteria, data and implications. *J. Geophys. Res.* **91,** 201–213 (1986).
29. Hess, P. C. On the source regions for mare picrite glasses. *J. Geophys. Res.* **105,** 4347–4360 (2000).
30. Anderson, O. L. The Gruneisen parameter for iron at outer core conditions and the resulting conductive heat and power in the core. *Phys. Earth Planet. Inter.* **109,** 179–197 (1998).
31. Stacey, F. D. & Anderson, O. L. Electrical and thermal conductivities of Fe-Ni-Si alloy under core conditions. *Phys. Earth Planet. Inter.* **124,** 153–162 (2001).
32. Stegman, D. R., Richards, M. A. & Baumgardner, J. R. Effects of depth dependent viscosity and plate motions on maintaining a relatively uniform MORB reservoir in whole mantle flow. *J. Geophys. Res.* **107,** doi:10.1029/2001JB000192 (2002).
33. Tackley, P. J. Effects of strongly variable viscosity on 3-dimensional mantle convection. *J. Geophys. Res.* **101,** 3311–3332 (1996).

Acknowledgements We thank B. Buffett for helpful discussions; C. Johnson, R. Jeanloz, M. Manga and H.-P. Bunge for comments; and D. Stevenson and M. Zuber for reviews that improved this manuscript. We dedicate this work to the memory of our co-author Stephen Zatman, who inspired us by his interest in this subject. This work was supported by IGPP LANL, NASA CT project, the National Science Foundation, and the Miller Institute for Basic Research in Science.

Competing interests statement The authors declare that they have no competing financial interests.

Correspondence and requests for materials should be addressed to D.S. (e-mail: dstegman@seismo.berkeley.edu).

Measuring intense rotation and dissipation in turbulent flows

Benjamin W. Zeff*, Daniel D. Lanterman*, Ryan McAllister*, Rajarshi Roy*, Eric J. Kostelich† & Daniel P. Lathrop*

* *Department of Physics, IPST and IREAP, University of Maryland, College Park, Maryland 20742-4111, USA*
† *Department of Mathematics, Arizona State University, Tempe, Arizona 85287-1804, USA*

Turbulent flows are highly intermittent—for example, they exhibit intense bursts of vorticity and strain. Kolmogorov theory[1,2] describes such behaviour in the form of energy cascades from large to small spatial and temporal scales, where it is dissipated as heat. But the causes of high intermittency in turbulence, which show non-gaussian statistics[3–5], are not well understood. Such intermittency can be important, for example, for enhancing the mixing of chemicals[6,7], by producing sharp drops in local pressure that can induce cavitation (damaging mechanical components and biological organisms)[8], and by causing intense vortices in atmospheric flows. Here we present observations of the three components of velocity and all nine velocity gradients within a small volume, which allow us to determine simultaneously the dissipation (a measure of strain) and enstrophy (a measure of rotational energy) of a turbulent flow. Combining the statistics of all measurements and the evolution of individual bursts, we find that a typical sequence for intense events begins with rapid strain growth, followed by rising vorticity and a final sudden decline in stretching. We suggest two mechanisms which can produce these characteristics, depending whether they are due to the advection of coherent structures through our observed volume or caused locally.

The problem of turbulence has been notoriously difficult to resolve, because it involves the interaction of flow length and timescales over many orders of magnitude. The intense, localized events that are characteristic of turbulence can cause difficulty in numerical simulations, via the generation of small scales and large local gradients. Simulations have some advantage in that they provide access to the entire field; alternatively, experiments can yield long observational records that are computationally impractical. Turbulence experiments also have limitations. Many measurements have relied on invasive techniques[9] that can affect the flow being studied. Usually, measurements do not capture the full three-dimensional nature of the flow; instead, they rely on one- or two-component approximations of velocities and velocity gradients. A fully three-dimensional (3D), spatially resolved technique is needed to measure important quantities such as the energy dissipation and helicity within the flow. Good temporal resolution is also required to study the rapid development of intense events.

A few recent experiments have captured many of these features. Tao *et al.*[10,11] used holographic particle image velocimetry (HPIV) to take elegant 3D snapshots of turbulent channel flow, though the technique is not time-resolved. Using two very different technologies, La Porta *et al.*[12] and Mordant *et al.*[13] tracked individual particles (a lagrangian measurement) in highly turbulent flows. This

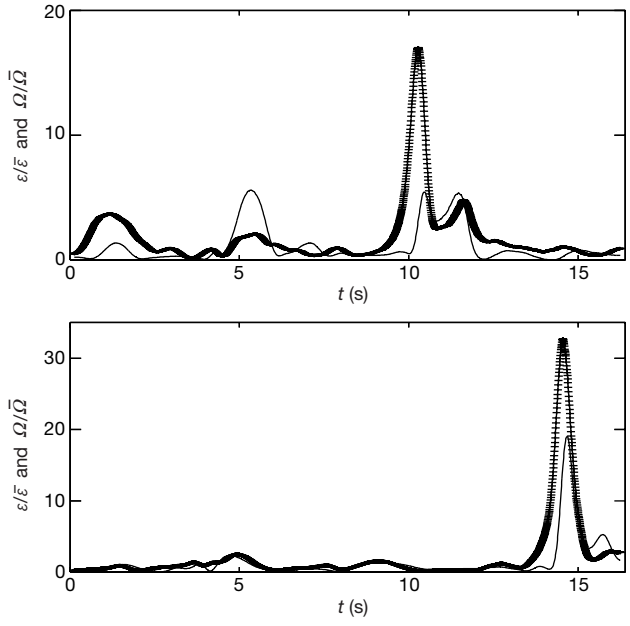

Figure 1 Time traces of the dissipation ε and enstrophy Ω. The two traces above show intense events occurring in a turbulent flow. Dissipation curves are marked with crosses, and enstrophy curves are shown as continuous curves. The time averages are $\bar{\varepsilon} = 0.0336\,\mathrm{cm^2\,s^{-3}}$ and $\bar{\Omega} = 4.13\,\mathrm{s^{-2}}$ with intermittent bursts reaching up to 40 times those values.

method provides direct access to the velocity and acceleration of the flow, but cannot yield velocity gradients.

We have designed and implemented a 3D particle image velocimetry technique[14] that obtains time series of the three components of velocity and all nine velocity gradients measured within a small volume. That is, this instrument allows us not only to study the statistics of intense, intermittent events, but also to observe and characterize their dynamics. In the following, we describe this technique and the results from a turbulent flow.

To visualize the 3D velocity field locally, we align three laser sheets such that each sheet illuminates one face of a small, cubic test volume, with the three sheets crossing at one vertex of the cube. The sheets illuminate 1 μm spherical polystyrene fluorescent particles that track the motion of the fluid. Three high-speed video cameras, recording at 125 frames per second, focus on the sheets, such that each camera sees only those particles in its own sheet. The key to reconstructing the 3D flow from these three slices is that the test volume be sufficiently small so that the flow within is, to good approximation, locally linear:

$$\mathbf{v} \approx \mathbf{b} + M\mathbf{x} \qquad (1)$$

where $M = \partial v_i/\partial x_j$ is the matrix of gradients. We use the two-dimensional velocity vectors from all three faces to estimate $\mathbf{b}$ and M for the whole cube. The dissipation ε and enstrophy Ω can be calculated at a given time step from the measured gradients: $\varepsilon = \nu\Sigma_{ij}(M_{ij} + M_{ji})^2/2$ and $\Omega = \Sigma_{ij}(M_{ij} - M_{ji})^2/4 = \boldsymbol{\omega}^2/2$, where $\boldsymbol{\omega} = \nabla \times \mathbf{v}$ is the vorticity and ν is the kinematic viscosity. In a turbulent flow, for equation (1) to hold, the test region must be of the order of, or smaller than, the Kolmogorov length η, the length scale at which viscosity smooths out the flow. We use three long-distance microscopes to image a small region (of size 1.8η), from a working distance of 43.3 cm.

Our flow is produced in a transparent cubic container of side $l = 22$ cm. Two square grids with a mesh size of $l_g = 0.85$ cm are rigidly connected to each other with a vertical spacing of 6.0 cm and are vertically oscillated with a position $y = y_0 \sin(\omega_g t)$ to drive the flow. The measurement volume at the centre of the tank is horizontally and vertically centred between the two grids.

The Reynolds number, which gives the approximate ratio of inertial to viscous forces in the flow, can be defined in terms of the tank size and the velocity amplitude of the grid, $\mathrm{Re} = l\omega_g y_0/\nu$; we present data for a flow with $\mathrm{Re} = 48,200$ and $R_\lambda = \nu^2_{x,\mathrm{rms}}/\nu\langle(\partial_x v_x)^2\rangle^{1/2} = 54$. The time average of the dissipation is $\bar{\varepsilon} = 0.0336 \ \mathrm{cm^2\,s^{-3}}$, which can be used to estimate the Kolmogorov length scale for this flow, $\eta = (\nu^3/\bar{\varepsilon})^{1/4} = 0.074$ cm.

To gather sufficient statistics, 5×10^6 sets of vectors and matrices for grid turbulence have been gathered, corresponding to 0.8 terabytes of video data. Video sequences of the flow reveal periods of unidirectional flow occasionally interrupted by visually striking vortices and hyperbolic flow patterns. Traces of ε and Ω (Fig. 1) reflect the intermittent nature of the flow. These distributions are qualitatively comparable to those observed in numerical simulations[15]. The probability distributions $\Pr(\varepsilon)$ and $\Pr(\Omega)$ (Fig. 2) both display long tails with high values more common for Ω than ε, indicating that vorticity is more intermittent than strain. Each component of the gradient matrix M assumes positive and negative values and, by continuity, must occasionally pass through zero. A one-dimensional approximation $\varepsilon \approx 15\nu(\partial_x u_x)^2$ of these quantities, as used in some previous experiments[3], implies that very low values of ε occur with much higher probability than we observe. In reality, it is unlikely that all nine gradient components simultaneously drop to zero.

Taken over the entire data set, the measure $\langle\varepsilon\Omega\rangle = 1.699\bar{\varepsilon}\bar{\Omega}$ indicates that these two quantities are not statistically independent. A scatter plot of ε versus Ω (Fig. 3) highlights the interdependence of these quantities. In particular, especially high values of ε coincide with high values of Ω sixteen times more frequently than if they were independent.

Our observations of the fluctuating gradients permit a statistical analysis of the interdependencies of the stretching and rotating parts of the field. It is useful to split the gradient matrix M into symmetric (representing strain) and antisymmetric (representing rotation) parts: $M = S + A$. Note that the dissipation is proportional to the sum of the squared components of S and that the enstrophy is proportional to the sum of the squared components of A. We observe that the time derivatives $\dot{\varepsilon}$ and $\dot{\Omega}$ are systematically affected by the local conditions of ε (and the three eigenvalues of S, which we denote as λ_i) and Ω. In particular, the dissipation on average is rising when the largest eigenvalue of S, λ_1, is large (see Fig. 4a), and falling when the enstrophy is large (see Fig. 4b).

The time dependence of the dissipation can be due to several

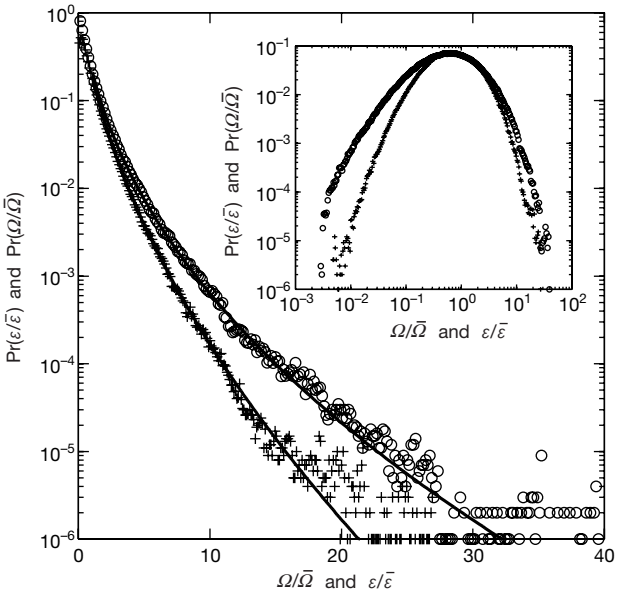

Figure 2 Distributions of the dissipation and enstrophy. The long tails of the probability distribution functions extend toward high values of ε (crosses) and Ω (circles), indicating that these are highly intermittent quantities. For values larger than their means, the distributions are well approximated by stretched exponentials, $\Pr(\varepsilon) \approx \exp[\varepsilon^{-0.62\pm0.08}]$ and $\Pr(\Omega) \approx \exp[\Omega^{-0.45\pm0.07}]$, as indicated by the solid lines. Inset, log–log plots show significant deviations from log-normality, which would yield parabolas here.

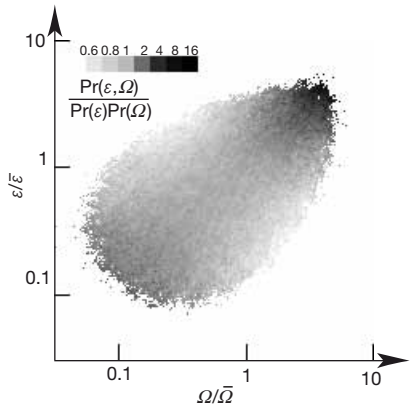

Figure 3 A scatter plot of dissipation versus enstrophy. The interdependence of these two quantities is clearly evident. The shading $\Pr(\varepsilon,\Omega)/\Pr(\varepsilon)\Pr(\Omega)$ would be 1 if ε and Ω are independent. While values close to their averages appear uncorrelated, high values of ε and Ω occur simultaneously about sixteen times more often than would be expected. Particularly low values appear similarly correlated. Only points with $\Pr(\varepsilon,\Omega) > 10^{-5}$ were plotted.

mechanisms. Although we will also advance the idea of local kinematic causes, another explanation invokes coherent structures being advected into our measurement volume. Because our observations are probably an admixture of the two phenomena, we will discuss interpretations relating to both.

Previous observations of vortex tubes with nearby sheets of high dissipation[16] offer one possible explanation to the behaviour seen in Fig. 1. An advecting velocity correlated with these structures is consistent with the observed statistics in the following way. Figure 4b shows the dissipation falling as the enstrophy increases. This is consistent with a dissipation decrease as the centre of a vortex core is approached, and that the high dissipation sheet precedes but does not trail the vortex. Figure 4c shows that the front of this preceding dissipation sheet would typically be compressive in two directions, while the back would have one compressive direction.

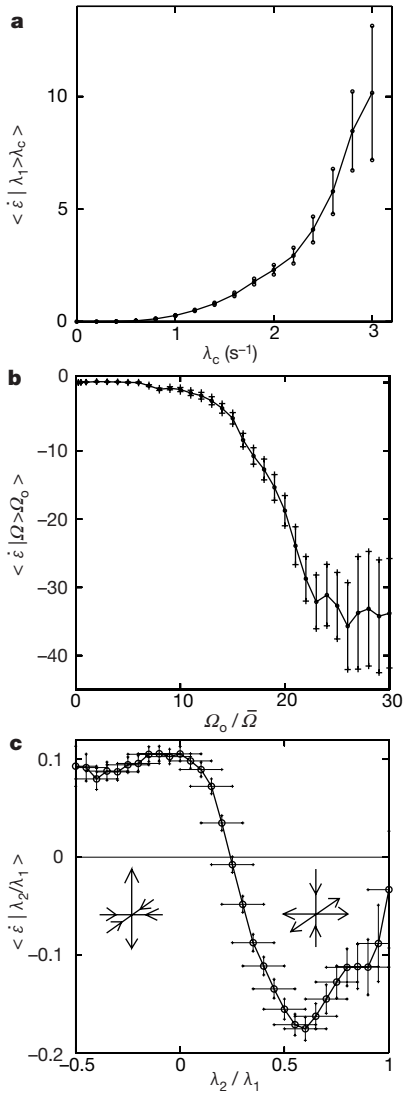

Figure 4 Conditional averages of the growth rate of dissipation $\dot{\varepsilon}$. **a**, The average of $\dot{\varepsilon}$ conditioned on the largest eigenvalue of the strain matrix λ_1 being larger than a value λ_c. Gradients, represented by λ_1, are subject to a self-steepening mechanism, causing the dissipation to rise. Note that $\varepsilon = 2\nu\Sigma_i\lambda_i^2$. **b**, The average of $\dot{\varepsilon}$ conditional on the enstrophy Ω being larger than a value Ω_0. The observations show an unambiguous decline in the dissipation when rotations are strong. We interpret this as a vortex 'squelch', whereby the vortices disrupt by mixing the self-steepening of the straining motions. **c**, The average of $\dot{\varepsilon}$ conditional on the ratio of the two largest eigenvalues of the strain matrix. Arrows indicate local flow stretching directions. The dissipation, on average, grows when there are two contracting directions, while for $\lambda_2/\lambda_1 > 0.25$ the dissipation, on average, falls. As the contracting directions are the ones unstable in growth by a Burger's mechanism, this may indicate that having two contracting directions enhances that mechanism.

We can learn about gradient fluctuations by studying our data and by examining the Navier–Stokes equations. If we expand the velocity field locally as a first-order Taylor series in $\boldsymbol{x}$, exactly as in equation (1), and substitute it into the Navier–Stokes equations, we obtain the following equation for $M : \dot{M} = -M^2 - \Pi/\rho$, where Π is the Hessian matrix for the pressure field[17]. This expansion neglects several factors, all quadratic in $\boldsymbol{x}$, including the effect of viscosity and the effect of advection in convecting gradients into our local region. This expression retains gradient steepening by the nonlinear term (M^2) and the nonlocal effect of pressure to enforce incompressibility. Note that Π is undetermined except by boundary conditions and incompressibility, $\mathrm{Tr}(M^2 + \Pi) = 0$; this is due to the nonlocality of the pressure. Finally, splitting M into symmetric and antisymmetric parts yields:

$$\dot{S} = -S^2 - A^2 - \Pi/\rho \tag{2}$$

$$\dot{A} = -SA - AS \tag{3}$$

These form a local basis for the interaction of rotation (A) and strain (S). Because the matrix A contains only the components of the vorticity, equation (3) gives $\dot{\boldsymbol{\omega}} = S\boldsymbol{\omega}$, indicating how the strains stretch and amplify vorticity[17].

The kinematics of equations (2) and (3) can be related to our observed statistics and by observations of events such as those displayed in Fig. 1.

First, the gradients show self-steepening instabilities, causing $\dot{\varepsilon} > 0$. These instabilities are probably of the same type that causes the gradients to grow in the Burger's equation. The conditional statistic shown in Fig. 4a substantiates this effect. Second, the presence of large gradients causes the vorticity to grow ($\dot{\Omega} > 0$) owing to the well-known vortex stretching mechanism. Finally, once the vorticity has grown, it causes the dissipation to fall, that is, $\Omega \gg \bar{\Omega}$ implies that $\dot{\varepsilon} > 0$, as is seen in Fig. 4b and anticipated in equation (2) (although the effect of the $-A^2$ term depends in a nontrivial way on the directions involved).

The events shown in Fig. 1 were chosen for their particularly large amplitudes of ε, but they show a sequence bearing out these three features. The gradients (as indicated by ε) first grow, in the absence of a large vorticity. Once the gradients are large, the vorticity (through Ω) shows a sudden, rapid increase. The peaking of the enstrophy is then accompanied by the rapid decline of the dissipation. We see no clear evidence, through conditional statistics, for a mechanism by which the vortices decline. It may be that slower viscous forces are required to damp the vortices, because kinematic mechanisms, as represented in equations (2) and (3), are ineffectual at damping vorticity.

Using this optical technique, we present these experiments to directly observe the development, interdependence and interaction of turbulent strain and vorticity. We have directly quantified intermittent events in the dissipation and enstrophy and discussed their relation to advecting structures. Our analysis includes a characterization of self-steepening and the first statistical evidence for vortex 'squelch' (see Fig. 4) of the dissipation. Our observations highlight how an understanding of the temporal interactions between stretching and vorticity is crucial to the science of extreme events in turbulence. □

Methods

Each image frame was broken into four 108 × 128 pixel subsections (9.7% overlap). A two-dimensional cross-correlation is performed between each subsection in subsequent images, a process which identifies the best two-dimensional pixel shift to particle images from one frame to the next. A weighted averaging technique is used to identify the cross-correlation peak to sub-pixel resolution, estimated at 0.25 pixels. A linear least-squares method fits the calculated velocity vectors and three-vector locations from each camera to the linear shear model of equation (1) to estimate **b** and M. Vector validation and

bootstrapping[18] are used to reduce the effect of spurious vectors caused by too few particles. The least-squares calculation is constrained to be divergence-free, that is, $\mathrm{Tr}(M) = 0$.

Received 11 July; accepted 26 November 2002; doi:10.1038/nature01334.

1. Kolmogorov, A. N. The local structure of turbulence in the incompressible viscous fluid for very large Reynolds numbers. *Dokl. Akad. Nauk. SSSR* **30,** 301–305 (1941); reprinted in *Proc. R. Soc. Lond. A* **434,** 9–13 (1991).
2. Kolmogorov, A. N. Dissipation of energy in the locally isotropic turbulence. *Dokl. Akad. Nauk. SSSR* **31,** 538–540 (1941); reprinted in *Proc. R. Soc. Lond. A* **141**, 15–17 (1991).
3. Sreenivasan, K. R. Fractals and multifractals in fluid turbulence. *Annu. Rev. Fluid. Mech.* **23,** 539–600 (1991).
4. Meneveau, C. & Sreenivasan, K. R. Simple multifractal cascade model for fully developed turbulence. *Phys. Rev. Lett.* **59,** 1424–1427 (1987).
5. Frisch, U. *Turbulence: The Legacy of A.N. Kolmogorov* 120–194 (Cambridge Univ. Press, Cambridge, 1995).
6. Gollub, J. P., Clarke, J., Gharib, M., Lane, B. & Mesquita, O. N. Fluctuations and transport in a stirred fluid with a mean gradient. *Phys. Rev. Lett.* **67,** 3507–3510 (1991).
7. Chaté, H., Villermaux, E. & Chormaz, J.-M. (eds) *Mixing: Chaos and Turbulence* (Kluwer Academic/Plenum, New York, 1999).
8. Kunns, K. T. & Papoutsakis, E. T. Damage mechanisms of suspended animal cells in agitated bioreactors with and without bubble entrainment. *Biotech. Bioeng.* **36,** 476–483 (1990).
9. Vukoslavcevic, P., Wallace, J. M. & Balint, J.-L. The velocity and vorticity vector fields of a turbulent boundary layer. Part 1. Simultaneous measurement by hot-wire anemometry. *J. Fluid Mech.* **228,** 25–51 (1991).
10. Tao, B., Katz, J. & Meneveau, C. Geometry and scale relationships in high Reynolds number turbulence determined from three-dimensional holographic velocimetry. *Phys. Fluids* **12,** 941–944 (2000).
11. Tao, B., Katz, J. & Meneveau, C. Statistical geometry of subgrid-scale stresses determined from holographic particle image velocimetery measurements. *J. Fluid Mech.* **457,** 35–78 (2002).
12. La Porta, A., Voth, G. A., Crawford, A. M., Alexander, J. & Bodenschatz, E. Fluid particle accelerations in fully developed turbulence. *Nature* **409,** 1017–1019 (2001).
13. Mordant, N., Metz, P., Michel, O. & Pinton, J.-F. Measurement of lagrangian velocity in fully developed turbulence. *Phys. Rev. Lett.* **87,** 214501 (2001).
14. Keane, R. D. & Adrian, R. J. Theory of cross-correlation analysis of PIV images. *Appl. Sci. Res.* **49,** 191–215 (1992).
15. Chen, S., Sreenivasan, K. R. & Nelkin, M. Inertial range scalings of dissipation and enstrophy in isotropic turbulence. *Phys. Rev. Lett.* **79,** 1253–1256 (1997).
16. Kida, S. & Ohkitani, K. Spatiotemporal intermittency and instability of a forced turbulence. *Phys. Fluids A* **4,** 1018–1027 (1992).
17. Majda, A. J. & Bertozzi, A. L. *Vorticity and Incompressible Flow* 6–13 (Cambridge Univ. Press, Cambridge, 2002).
18. Kostelich, E. J. Bootstrap estimates of chaotic dynamics. *Phys. Rev. E* **64,** 016213 (2001).

Acknowledgements We gratefully acknowledge the support of the National Science Foundation and the Research Corporation. R.M. and R.R. gratefully acknowledge support from the Office of Naval Research (Physics Division). We thank D. Levermore, J. Rodgers, D. DeShazer, K. R. Sreenivasan, E. Ott, T. Antonsen and J. Fineberg for advice.

Competing interests statement The authors declare that they have no competing financial interests.

Correspondence and requests for materials should be addressed to D.P.L. (e-mail: dpl@complex.umd.edu).

Observation of surface and bulk phase transitions in nematic liquid crystals

M. I. Boamfa, M. W. Kim, J. C. Maan & Th. Rasing

NSRIM Institute and High Field Magnet Laboratory, University of Nijmegen, Toernooiveld 1, 6525 ED, Nijmegen, The Netherlands

The behaviour of liquid crystal (LC) molecules near a surface is of both fundamental and technological interest: it gives rise to various surface phase-transition and wetting phenomena[1–14], and surface-induced ordering of the LC molecules is integral to the operation of LC displays[15,16]. Here we report the observation of a pure isotropic–nematic (IN) surface phase transition—clearly separated from the bulk IN transition—in a nematic LC on a substrate. Differences in phase behaviour between surface and bulk are expected[1–4], but have hitherto proved difficult to distinguish, owing in part to the close proximity of their transition temperatures. We have overcome these difficulties by using a mixture of nematic LCs: small, surface-induced composition variations lead to complete separation of the surface and bulk transitions, which we then study independently as a function of substrate and applied magnetic field. We find the surface IN transition to be of first order on surfaces with a weak anchoring energy and continuous on surfaces with a strong anchoring. We show that the presence of high magnetic fields does not change the surface IN transition temperature, whereas the bulk IN transition temperature increases with field. We attribute this to the interaction energy between the surface and bulk phases, which is tuned by magnetic-field-induced order in the surface-wetting layer.

In a confined geometry, interactions between LC molecules and the surfaces of the confining walls give rise to different LC behaviour at the surface and in the bulk. Upon undergoing the IN transition the delicate balance of intermolecular interactions tends to favour the LC–surface interaction in the nematic phase, whereas the LC–LC interaction tends to dominate in the isotropic phase. The new nematic phase therefore occurs first at the surface, a phenomenon known as "wetting"[1,2,13,14]. The IN transition is relatively weak thermodynamically, so large pre-transitional effects take place before the transition. The interaction of these pre-ordered LC molecules with the surface is known as "pre-wetting"[2,13,14]. In a magnetic field the diamagnetic LC molecules undergo a torque that forces them to orient relative to the field direction[17]. Although at the level of individual molecules the magnetic field effect is negligibly small in the isotropic phase, the collective behaviour of the mesophase causes the molecular contribution to add up constructively, resulting in a macroscopic orientation effect (Fig. 1).

A variety of theoretical studies have addressed this wetting problem either at the general level of surface-related phenomena[1,2] or for LCs in particular[3,4]. Cahn[1] introduced a first-order wetting transition leading to an ordering film of finite thickness in any two-phase mixture of fluids contacting a third phase at a critical temperature. Later, Nakanishi and Fisher[2] showed that pre-wetting of a highly ordered film with finite thickness on a surface continues to wetting via a first-order or continuous wetting transition. This pre-wetting, where a strongly anchored LC layer forms a uniform nematic phase adjacent to the substrate and near the isotropic bulk, has often been discussed for the case of strong surface fields[3,4].

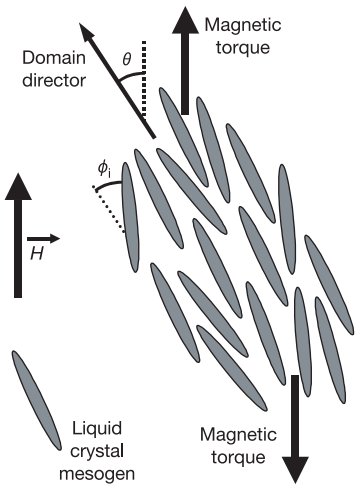

Figure 1 A correlated volume of liquid crystal mesogenes under the influence of an applied magnetic field, **H**. The field tends to orient the domain as a whole, changing the director orientation relative to the field, θ, leaving unchanged the individual molecules within the domain, ϕ_i.